Editors' Suggestion

Ionic liquid drop impact onto heated surfaces

Lihui Liu,[1] Bijiao He,[1] Weizong Wang,[1] Guobiao Cai,[1,*] and Peichun Amy Tsai[2,†]
[1]*School of Astronautics, Beihang University, Beijing 100191, China*
[2]*Department of Mechanical Engineering, University of Alberta, Edmonton, Alberta T6G 2G8, Canada*

(Received 28 November 2022; accepted 24 May 2023; published 13 July 2023)

Ionic liquids (ILs), molten salts at low temperatures, are nonionizing, thermally stable, and with low vapor pressure, thereby offering promising applications for lubrication, cooling, and combustion, where drop impact on a heated surface plays a vital role. Drop impact on heated surfaces has been extensively investigated with molecular liquid drops, such as water and ethanol, but rarely explored with ILs. We experimentally investigate the impact dynamics of three types of IL drops onto a heated flat surface under broad ranges of impact velocity ($0.18 \leqslant U \leqslant 4.22$ m/s) and surface temperature ($18 \leqslant T_s \leqslant 455\,^{\circ}$C). The impact events observed with the ILs include spreading, spreading with bubbling, and splashing with bubbling. However, the dynamic Leidenfrost effect with an insulating vapor film causing droplet rebound, typically recorded for molecular liquid drops under an initial impact velocity, is not observed for the IL liquids under similar Weber number ($\mathrm{We} \approx 2$) and surface temperature (at $T_s = 350\,^{\circ}$C). This suppression is attributed to the low gas pressure underneath the IL droplet, induced by evaporation and thermal decomposition of ILs, and can significantly benefit various thermal applications such as cooling and coating. Finally, the maximum spreading factor of the IL drops is modeled using an energy conservation concept and is consistent with experimental results.

DOI: 10.1103/PhysRevFluids.8.073602

I. INTRODUCTION

The fundamentals of drop impact dynamics on heated surfaces crucially affect a variety of applications, for example, cooling [1–4], coating [5,6], and combustion [7–9]. Researchers have extensively worked on molecular droplets, e.g., water, ethanol, and diesel, impacting on heated surfaces [10–13]. The impact dynamics and outcomes on heated surfaces are significantly influenced by droplet properties, for instance, the Weber number [14] and saturation temperature [15–18], surface parameters (e.g., temperature [15–18], textures and roughness [19–24]), as well as ambient pressure [25]. Due to evaporation and boiling, distinct impact events of secondary atomization [16], central jetting [22–24], and break-up [23,24] are triggered as droplets undergo phase changes when impacting heated surfaces.

When a droplet (with a negligible impact velocity) gently deposits on heated surfaces where the surface temperature (T_s) is far greater than the liquid saturation temperature, the droplet can be levitated by a vapor cushion generated by evaporation, preventing the droplet from physically contacting the heated surface, known as the (static) Leidenfrost effect [26]. As a droplet impacts (with an initial velocity) on high-T_s surfaces, the vapor cushion could exist and possibly induces a complete rebound, termed the dynamic Leidenfrost effect [27–31]. Such an intervening vapor film can benefit drag reduction [32] but impede heat transfer [33]. The corresponding critical surface

*cgb@buaa.edu.cn
†peichun.amy.tsai@ualberta.ca

TABLE I. Density (ρ), surface tension (σ), dynamic viscosity (μ), and decomposition temperature (T_{onset}) of the ionic liquids at standard pressure and temperature (20 °C).

Liquids	Density, ρ (kg/m^3)	Surface tension, σ (mN/m)	Dynamic viscosity, μ (mPa s)	Decomposition temperature, T_{onset} (°C)
[EMIM][SCN]	1120	36.1	33	242
[EMIM][BF4]	1280	44.1	39	412
[BMIM][PF6]	1350	42.5	304	385
Milli-Q water	998	72.0	1	$T_b = 100$[a]

[a]T_b is the saturation temperature of Milli-Q water.

temperature, known as the Leidenfrost point, can be influenced by structured thermal armors [33], micro/nanotextures [34], roughness [35], surfactants [36], and electric fields [37].

Ionic liquids (ILs), comprised of cations and anions, are nonmolecular liquids and known as molten salts at low temperatures. ILs are generally poor to moderate electrical conductors, nonionizing, and thermally stable and frequently exhibit low vapor pressure [38,39]. Moreover, ILs have a significant advantage in terms of design ability due to the substantial combination possibilities of cations and anions [40], making them suitable candidates in the applications of combustion, cooling, and coating [39–42]. Unlike molecular liquids, evaporation and/or decomposition could occur as the temperature of ILs increases [39,42]. The boiling and evaporation of molecular liquids (such as water and ethanol) is a physical process, whereas the thermal decomposition of ILs is a chemical process. Therefore, the impact dynamics of ILs may considerably differ from those of molecular liquids and hence warrants systematic investigations. However, to the best of our knowledge, there is only one study reporting the spreading of an ionic liquid (1-ethyl-3-methylimidazolium acetate, [Emim]Ac) drop impacting on a mildly heated solid surface ($T_s \leqslant 110$ °C) [43].

Here we examine the impact dynamics of ILs drops impacting on flat heated glass. The impact outcomes of spreading, bubbling, and splashing are observed under our experimental conditions. However, events like break-up, secondary atomization, and Leidenfrost effect, typically observed with molecular liquids, are suppressed by the ILs utilized because of their thermal stability and the low gas pressure produced by evaporation and thermal decomposition. Furthermore, the maximum spreading factor of IL drops is theoretically modeled and validated experimentally.

II. EXPERIMENTAL

The experiments of drop impact were conducted under the room temperature of 18 °C and an atmospheric pressure of 101 kPa. Three kinds of ionic liquid, [EMIM][SCN] (1-ethyl-3-methylimidazolium thiocyanate), [EMIM][BF4] (1-ethyl-3-methylimidazolium tetrafluoroborate), and [BMIM][PF6] (1-butyl-3-methylimidazolium hexafluorophosphate) (Monils Chem.), were utilized. To obtain the pure ionic liquid (>99%), they were left in a vacuum ($\approx$ 1 Pa) for 24 hr to remove impurities, e.g., gas and water. The density (ρ), surface tension (σ), dynamic viscosity (μ), and decomposition temperature (T_{onset}) of the ionic liquids are listed in Table I. We used the same methods and procedures as Ref. [44] for measuring σ and μ. A blunt needle (20G) and a syringe pump (Chemyx fusion 200) were used to generate single droplets. A droplet detaches from the needle when its weight overcomes the surface tension, forming a uniform initial diameter (D_0). The droplet then free falls from an initial height ranging from 5 to 1000 mm. The impact velocity range is 0.18 m/s $\leqslant U \leqslant$ 4.22 m/s, determined by image analysis of tracking the droplet displacement varying with time. The Weber number ($\text{We} = \rho U^2 D_0/\sigma$) and Reynolds ($\text{Re} = \rho U D_0/\mu$) number ranges explored are $2 \leqslant \text{We} \leqslant 1377$ and $2 \leqslant \text{Re} \leqslant 376$, respectively, The former compares the drop's kinetic to surface energy, whereas the latter characterizes the inertia to viscous effect. The values of We and Re are estimated using the liquid properties at standard pressure and temperature (20 °C) unless they are specified differently. The solid surface is a flat silica glass heated by a

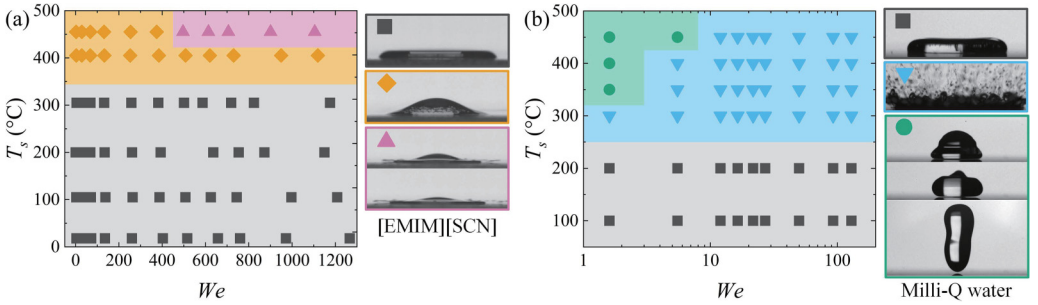

FIG. 1. Phase diagrams of (a) [EMIM][SCN] ionic liquid and (b) Milli-Q water drops impacting on heated glass at a wide range of Weber number (We) and surface temperature (T_s). (b) Reconstructed from Ref. [16] for comparison. The impact outcomes of spreading (■), spreading with bubbling (◆), and splashing with bubbling (▲) are observed with [EMIM][SCN] drops, and spreading (■), complete rebound (i.e., dynamic Leidenfrost effect) (●), and spreading with atomizating (▼) with Milli-Q water drops. We is calculated using drop properties at standard pressure and temperature. The errors in We and T_s are ≈ 6.7% and 5 °C, respectively.

customized heater, and the glass temperature range is $18\,^{\circ}\mathrm{C} \leqslant T_s \leqslant 455\,^{\circ}\mathrm{C}$. The glass surface is replaced by a fresh one after each test to guarantee cleanness. A high-speed camera (Photron Nova S12) is utilized to capture the side view of impact dynamics at 12 800 fps. Further experimental details are described in the Supplemental Material [45].

III. RESULTS AND DISCUSSION

Figure 1(a) shows the phase diagram and representative snapshots of [EMIM][SCN] drops impacting on a heated glass under various We and T_s. The resulting impact outcomes comprise spreading, spreading with bubbling, and splashing with bubbling, and their sequential snapshots are displayed in Fig. S2 [45]. In comparison, the splashing with bubbling is not observed with [EMIM][BF4] and [BMIM][PF6] (see Fig. S4 [45]), which will be discussed later. The phase diagram of Milli-Q water drops under similar conditions is reconstructed from our previous study [16] for comparison. Milli-Q water is simply water purified using a Millipore Milli-Q laboratory water system to possess consistent ionic purity (with an electrical resistivity of 18.2 MΩ cm at 25 °C); its properties are listed in Table I. As shown in Fig. 1(b), the impact outcomes of water drops can be classified into spreading, complete rebound (i.e., dynamic Leidenfrost effect), and spreading with atomizating.

Spreading is the sole observed impact event for all IL drops explored as T_s is less than or marginally above T_{onset}. The IL droplets spread first, retract after reaching the maximum spreading diameter, and adhere to the glass surface. With IL droplets, due to their thermal stability, we do not observe the typical events of bubbling within the droplet and secondary atomization outside the droplet (due to the boiling and evaporation) at relatively high T_s (>250 °C), as typically seen with the molecular liquid [15,23] [Fig. 1(b)].

When T_s is greater than T_{onset}, spreading with bubbling is observed with all IL drops utilized. The bubbles appear inside the IL droplets during impact, as shown in Fig. 1(a). ILs generally degrade above T_{onset}, undergoing so-called thermal decomposition [40]. Most of the thermal decomposition processes of ILs are the substituent reaction between an anion and a cation [40], and the decomposition product comprises volatile gases [39]. The bubbles (recorded inside the IL droplets) are caused by the volatile gas generated at the liquid-surface interface. Meanwhile, smoke as the decomposition product of ILs is observed, as illustrated by the representative snapshot in Fig. 1(a) and close-up snapshots (Fig. S3 [45]). Sporadic and tiny secondary droplets exist around the main body, similar to the secondary atomization caused by molecular liquids (Milli-Q water) on heated surfaces [Fig. 1(b)]. However, the number, density, and diameter of secondary droplets

of ILs due to chemical decomposition are far less than those of the molecular liquids due to boiling and evaporation.

Under high We and T_s ranges, splashing occurs with [EMIM][SCN] droplets, with small values of surface tension and viscosity (see Table I). Conversely, splashing is hardly observed with [EMIM][BF4] and [BMIM][PF6] under the conditions explored (see Fig. S4 [45]), suggesting that the lower the surface tension and viscosity, the easier it is to trigger the splashing, consistent with the molecular liquid case [46]. In low-T_s range, the splashing is absent within the We range explored for all the ILs under our experimental conditions. Since ILs are generally viscous, splashing can be expected at a significantly high impact velocity at the low-T_s range for ILs, which should be greater than the current maximum impact velocity (4.22 m/s) in our study. The droplet viscosity exponentially reduces with the increase of temperature [see Eq. (4)]. Hence, at the high-T_s range, we can observe the splashing with [EMIM][SCN] droplets at a moderate impact velocity [at 2.71 m/s shown in Fig. 1(a)].

As illustrated by Fig. 1(b) inset, the dynamic Leidenfrost effect exhibiting a complete rebound is recorded with the Milli-Q water drop at the low-We and high-T_s range. The water drop deposits, spreads, retracts, and rebounds on an insulating vapor film, eventually leading to a complete rebound. However, the dynamic Leidenfrost effect is not observed for ILs drops in the We and T_s ranges explored. The occurrence of the Leidenfrost phenomenon can be determined by whether the gas pressure (underneath the droplet), P_g, generated by the evaporation and the decomposition of ILs can overcome the droplet's dynamic impact pressure ($P_d \sim \rho U^2$) [22,23,27]. We will now estimate P_g and P_d to explain the absence of the dynamic Leidenfrost effect under our conditions.

To estimate the gas pressure (P_g) underneath Leidenfrost droplets, the deformed droplet is simplified as a disk sitting on a flatted incompressible gas layer with a height of h_g. The disk diameter is approximated using the maximum spreading diameter of the droplet (D_m), and the disk height (H) can be calculated from volume conservation, $D_0^3 \sim D_m^2 H$. As experimentally revealed in Refs. [28,47], h_g approximately ranges from 1 μm to 100 μm, leading to $h_g/D_m \ll 1$. Accordingly, the lubrication approximation, $P_g/D_m = \mu_g U_g/h_g^2$, can be utilized to evaluate P_g, where μ_g and U_g are the gas dynamic viscosity and average escaping velocity, respectively. The gas mass flow rate caused by the escaping is expressed by $\dot{m} \sim \rho_g U_g h_g D_m$, where ρ_g stands for the gas density. The gas pressure hence scales with

$$P_g \sim \frac{\mu_g}{\rho_g}\frac{\dot{m}}{h_g^3}. \tag{1}$$

The gas dynamic viscosity (μ_g) and density (ρ_g) slightly change with the gas species (generally in the same order of magnitude for the different gas species). Consequently the gas pressure (P_g) is primarily determined by $\dot{m}$ and h_g, as revealed by Eq. (1).

During the dynamic Leidenfrost event, the droplet retracts after achieving its maximum spreading diameter and then rebounds off the heated surface. The droplet's retraction is influenced by capillary force [$F_c \sim (\sigma/H)D_m^2$] and the viscous force [$F_g \sim \mu_g(U_g/h_g)D_m^2$] exerted by the gas layer. A decrease in surface tension reduces F_c. Qualitatively, F_g is supposed to be reduced when F_c decreases, thereby increasing h_g. Some research effort has been devoted to correlating the h_g with drop properties [27,31,48,49]. Shirota *et al.* [27] studied the length scale of the dynamic Leidenfrost effect and proposed $h_g \sim D_0(\mathrm{St})^{-2/3}$, where $\mathrm{St} = \rho D_0 U/\mu_g$ is the Stokes number. This relation can be expressed in terms of the Weber number, $h_g \sim D_0(\rho D_0 U/\mu_g)^{-2/3} = D_0(1/\mathrm{We})^{2/3}(\mu_g U/\sigma)^{2/3}$. Hence, at the same Weber number, h_g is inversely proportional to the drop surface tension (σ). Gauthier *et al.* [47] experimentally measured the gas layer height underneath the static Leidenfrost drops levitating on a heated spinning surface. Two liquids with the same viscosity but different surface tension, silicone oil (21 mN/m) and a mixture of glycerol and water (64 mN/m), were utilized. The measured results [Fig. 2(c) in Ref. [47]] indicate that the thin-film layer height for silicone oil is larger than that for the glycerol mixture under the same conditions. Another theoretical analysis shows that the gas layer height inversely correlates with the surface tension for the static Leidenfrost drops [50]. By the same token, here we assume that the similar relationship of lower

σ leading to a higher h_g (shown in the above Leidenfrost observations) holds for the dynamic Leidenfrost event.

To estimate $\dot{m}$ in Eq. (1), we assume $\dot{m}$, resulting from the escaping gas underneath the droplet, is balanced by the gas generated by the IL evaporation/decomposition during the dynamic Leidenfrost event. More specifically, volatile gas is generated because of the evaporation and decomposition when the ILs temperature rises [39]. ILs thermally decompose via a reaction of one cation with one anion, and the concentrations of cations and anions in the bulk ionic liquid remain constant. The decomposition rate (w_d) can be expressed in terms of the molar proportion of the ionic liquid that has decomposed as a function of time using the Arrhenius equation [51]:

$$w_d = A_k \exp\left(\frac{-E_a}{RT_d}\right), \tag{2}$$

where A_k is the prefactor with the unit of time (min^{-1}), E_a is the activation energy, R is the universal gas constant, and T_d is the droplet temperature. When the contribution of evaporation is assumed to be small, overall A_k and E_a encompassing both evaporation and decomposition can be determined from the thermogravimetric analysis [39]. We hence assume that the maximum gas mass flow rate produced by the evaporation and decomposition of the ILs can be estimated by Eq. (2).

Considering the evaporation contribution of molecular liquid drops, the thermal transfer through conduction during the Leidenfrost effect can be modeled using Fourier's law, $\dot{Q} = \lambda \Delta T A/h$, where λ is the thermal conductivity of the vapor, h is the height of the vapor layer, $A \approx \pi(D_0/2)^2$ is the cross-sectional surface area, and ΔT is the temperature difference between the droplet (T_d) and solid surface. Hence, the gas mass flow rate, $\dot{m}$, caused by the evaporation can be approximated as $\dot{m} = \lambda \Delta T A/(hL)$, where L is the latent energy [23,52]. $\dot{m}$ can then be expressed in terms of the mass proportion (w_e) due to evaporation:

$$w_e = \frac{\dot{m}}{m} = \frac{3\lambda \Delta T}{2\rho h L D_0}, \tag{3}$$

where $m = \rho \pi D_0^3/6$ is the initial mass of the droplet.

As shown in Fig. 1(b), a dynamic Leidenfrost effect exhibiting complete rebound is observed when a Milli-Q water droplet with We = 2 ($D_0 = 2.35$ mm and $U = 0.22$ m/s) impacts on a heated surface at $T_s = 350\,^\circ$C and $T_s = 400\,^\circ$C, but not at $T_s = 300\,^\circ$C. The thermal conductivities of water vapor at $T_s = 300\,^\circ$C, $350\,^\circ$C, and $400\,^\circ$C are $\lambda = 0.044$, 0.049, and 0.055 W/(m K), respectively [53]. Here we assume that h holds constant at $300\,^\circ\text{C} \leqslant T_s \leqslant 400\,^\circ$C. According to the experimental measurement with x-ray imaging for dynamic Leidenfrost drops [28], we approximate $h \approx 50$ μm. With the conditions of $D \approx D_0$ and $\Delta T = T_s - T_d \approx T_s$ assuming the drop temperature T_d is much smaller than T_s, the gas mass flow rate is calculated to be $w_e \approx 7.4 \times 10^{-2}$ s^{-1}, $w_e \approx 9.7 \times 10^{-2}$ s^{-1}, and $w_e \approx 1.24 \times 10^{-1}$ s^{-1} at $T_s = 300\,^\circ$C, $350\,^\circ$C, and $400\,^\circ$C, respectively. Using Milli-Q water drop data, the criterion of gas mass flow rate for the appearance of the dynamic Leidenfrost effect (or for the gas pressure overcoming the dynamic pressure, i.e., $P_g = P_d$) under We = 2 and $T_s = 350\,^\circ$C would be $w_e \approx 10^{-1}$ s^{-1}.

Taking [BMIM][PF6] as an example, its experimental measured properties are $A_k \sim O(10^{10})$ min^{-1} and $E_a = 137.8$ kJ/mol [39,40]. Although there have been several studies on temperature variation of droplets on heated surfaces [1,16,17,54], a precise relation between T_d and T_s is unavailable theoretically and experimentally so far since it is challenging to measure T_d accurately using direct methods, especially during the ultrafast dynamics of drop impact and spreading. The previous work [1,16–18] pointed out that T_d varies with the impact time, impact velocity, thermal effusivity, specific heat capacity, surface temperature, etc., implying a complicated relationship between T_d and T_s. Taking into account the fact that T_d is always lower than T_s, the maximum gas mass flow rate can be estimated with Eq. (2) by replacing T_d with T_s since w_d is proportional to T_d. The maximum gas mass flow rate of [BMIM][PF6] induced by decomposition and evaporation is estimated to be $w_d \approx 4.7 \times 10^{-4}$ s^{-1} at We = 2 and $T_s = 350\,^\circ$C.

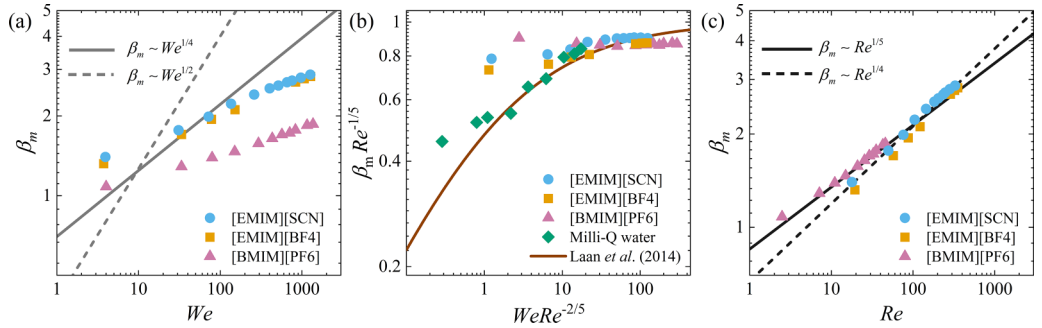

FIG. 2. Variation of the maximum spreading factor ($\beta_m = D_m/D_0$) of ionic liquid drops with the (a) Weber number (We), (b) impact parameter of $p \equiv \mathrm{WeRe}^{-2/5}$ defined by Laan *et al.* [55], and (c) Reynolds number (Re) at a surface temperature of $T_s = 18\,^\circ$C. The values of We and Re are estimated using drop properties at standard pressure and temperature. The error of the measured β_m is ≈3%.

At the same conditions (We = 2 and $T_s = 350\,^\circ$C), the gas mass flow rate ($w_d \sim 10^{-4}$ s^{-1}) of [BMIM][PF6] drops is significantly less than that of Milli-Q water drops ($w_e \sim 10^{-1}$ s^{-1}), but h_g of the [BMIM][PF6] drops is higher than that of Milli-Q water drops due to the low surface tension. Therefore, on the one hand, P_g underneath the [BMIM][PF6] drops is at least three orders of magnitude lower than that of Milli-Q water drops at the same conditions, as revealed by Eq. (1). On the other hand, the dynamic pressure can be expressed using the Weber number, $P_d \sim \rho U^2 = \mathrm{We}\sigma/D_0$. At the same We, the dynamic pressure of water and IL drops is slightly different but on the same order of magnitude. Therefore, $P_g \ll P_d$ is estimated for ILs drops at We = 2 and $T_s = 350\,^\circ$C, and accordingly the dynamic Leidenfrost effect could not be observed for the ILs used. Nonetheless, for a broad spectrum of ILs, it may still be possible to observe the dynamic Leidenfrost effect, especially for a large A_k combined with a small E_a, as suggested by Eq. (2).

Overall, the impact events of the break-up, massive secondary atomization, and Leidenfrost effect, typically observed for molecular liquid droplets impacting a flat heated surface [15,16], were absent with IL drops benefiting from the thermal stability.

We now examine the IL drops' maximum spreading factor (β_m), defined as $\beta_m = D_m/D_0$, the ratio of the maximum spreading diameter (D_m) to the initial droplet diameter (D_0). Figure 2 shows the variation of β_m with We and Re for different ionic liquids at $T_s = 18\,^\circ$C. Various theoretical models exist concerning the dependence of β_m on various parameters in the literature [55–58]. For example, an energy-conservation model of $\beta_m \sim \mathrm{We}^{1/2}$ [55,56] is proposed by assuming that the kinetic energy of the droplet is completely converted into surface energy as D_m is reached. Differently, Clanet *et al.* [56] theoretically derived $\beta_m \sim \mathrm{We}^{1/4}$ from the momentum and volume conservation perspective, which is in good agreement with the experimental data of low-viscous Milli-Q water [23,56]. However, the results in Fig. 2(a) indicate that the trend of the IL drops' β_m deviates from these classical power laws of $\beta_m \sim \mathrm{We}^{1/4}$ and $\beta_m \sim \mathrm{We}^{1/2}$ because ILs are generally more viscous than water (by ≈30× to 300×; see Table I).

In addition, Laan *et al.* [55] proposed a universal scaling law of $(D_m/D_0)\mathrm{Re}^{-1/5} = p^{1/2}/(A + p^{1/2})$ using the impact parameter of $p \equiv \mathrm{WeRe}^{-2/5}$, where A is a fitting constant. The impact parameter p is introduced to distinguish the two asymptotic regimes, namely, the inviscid regime ($p \ll 1$) and the high-viscous regime ($p \gg 1$). The fluid viscosity dominates the spreading in the high-viscous regime, while the capillarity dominates in the inviscid regime. The scaling law is deduced as $\beta_m \sim \mathrm{We}^{1/2}$ and $\beta_m \sim \mathrm{Re}^{1/4}$ for the inviscid regime and the high-viscous regime through energy conservation, respectively. Between the two asymptotic regimes, a smooth crossover is constructed using a Padé approximant, yielding $(D_m/D_0)\mathrm{Re}^{-1/5} = p^{1/2}/(A + p^{1/2})$ [55]. Our experimental results using IL drops are consistent with the above model by Laan *et al.* within

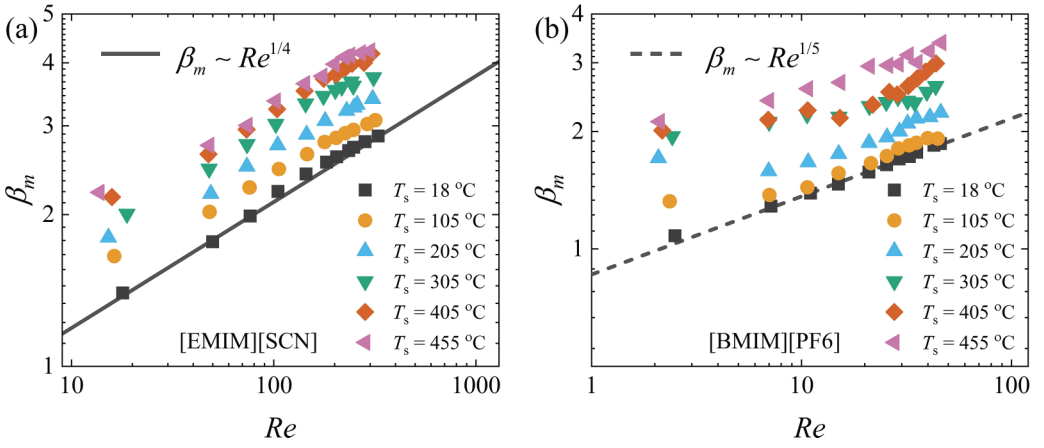

FIG. 3. Variation of the maximum spreading factor ($\beta_m = D_m/D_0$) of (a) [EMIM][SCN] (with a low viscosity) and (b) [BMIM][PF6] (with a high viscosity) with the Reynolds number, Re, estimated using drop properties at standard pressure and temperature, for different surface temperatures (T_s). The error of the measured β_m is ≈3%.

a specific impact parameter range ($10 < p < 100$) for the low-viscosity ILs ([EMIM][SCN] and [EMIM][BF4]), as shown in Fig. 2(b).

A classic scaling law of $\beta_m \sim \sqrt{(\mathrm{We}+12)/[3(1-\cos\theta_a)+4\mathrm{We}/\sqrt{\mathrm{Re}}]}$ is derived by Pasandideh-Fard *et al.* [57], where θ_a is the advancing contact angle, by assuming that the initial kinetic energy is dissipated by viscosity as the droplet reaches the maximum spreading diameter. This scaling law is deduced by assuming that the viscosity dissipation occurs over a boundary layer at the liquid-solid interface, rather than in the whole drop body, as shown in Ref. [57] (Fig. 10) and Ref. [58] (Fig. 8). Under $\mathrm{We} \gg \sqrt{\mathrm{Re}}$ and $\mathrm{We} \gg 12$, the above scaling law is approximated as $\beta_m \sim \sqrt{\mathrm{We}/(4\mathrm{We}/\sqrt{\mathrm{Re}})} \sim \mathrm{Re}^{1/4}$ [57]. ILs are generally viscous, and $\mathrm{We} \gg \sqrt{\mathrm{Re}}$ ($\mathrm{We}/\sqrt{\mathrm{Re}} = \sqrt{\mathrm{We}\mu U/\sigma} \gg 1$) is readily satisfied at $\mathrm{We} \gg 12$. In agreement, the experimental results of [EMIM][SCN] droplets (with a low viscosity, $\mu = 33$ mPa s) are consistent with $\beta_m \sim \mathrm{Re}^{1/4}$, as shown in Fig. 2(c). The viscosity of [EMIM][SCN] and [EMIM][BF4] is similar, and thus their experimental variation of β_m is nearly identical [shown in Fig. 2(c)].

However, for the high-viscosity liquids, we consider that the viscosity dissipation can exist over the whole drop and scales with $\mu U D_m^3/H$, where H is the drop thickness. The conservation of both energy and volume ($\pi D_0^3 \sim \pi D_m^2 H$) yields $\beta_m \sim \mathrm{Re}^{1/5}$ [56]. Given the high dynamic viscosity of [BMIM][PF6] ($\mu = 304$ mPa s) the spreading of [BMIM][PF6] droplets is primarily dominated by viscous force, as anticipated, conforming to the relationship $\beta_m \sim \mathrm{Re}^{1/5}$, as shown in Fig. 2(c).

Figure 3 shows the variation of β_m of [EMIM][SCN] (with a low viscosity) and [BMIM][PF6] (with a high viscosity) with Re at the different T_s, suggesting that the trends of β_m varying with Re are nearly identical under the same T_s. Tran *et al.* [15] experimentally fitted $\beta_m \sim \mathrm{We}^{2/5}$ for the molecular liquid drops (Milli-Q water and FC-72) impacting on flat heated surfaces. We previously established an empirical model for Milli-Q water drops impacting on flat heated surfaces using energy conservation [23], similar to that of Wildeman *et al.* [59], showing that the initial drop surface energy plus 75% of the initial drop kinetic energy are transferred into the final surface energy. The viscosity of ILs is higher than that of Milli-Q water and FC-72. Hence, these power laws of β_m for molecular liquids in the literature may not be applicable to the IL drop spreading on heated surfaces, as shown in Fig. 3.

Figure 3 also reveals increasing β_m with rising T_s as the IL viscosity decreases due to increasing T_d on a heated surface. The dynamic viscosity of the ILs decreases exponentially with temperature

(see Fig. S5 [45]). The viscosity dissipation decreases with increasing T_s, thereby enlarging β_m. The slopes of β_m at the different T_s for both [EMIM][SCN] and [BMIM][PF6] approximately take a constant and are 1/4 and 1/5, respectively. The data strongly suggest that the scaling laws of β_m at different T_s can be expressed as $\beta_m(T_s) \sim \mathrm{Re}(T_d)^{1/4}$ and $\beta_m(T_s) \sim \mathrm{Re}(T_d)^{1/5}$ for [EMIM][SCN] and [BMIM][PF6], respectively. Here $\mathrm{Re}(T_d)$ refers to the droplet Reynolds number calculated with the properties at the droplet temperature of T_d, while T_d strongly depends on the surface temperature of T_s and impact dynamics.

The droplet Reynolds number at the droplet temperature T_d can be calculated from $\mathrm{Re}(T_d) = \rho(T_d)UD_0/\mu(T_d)$, where $\rho(T_d)$ and $\mu(T_d)$ stand for the droplet density and dynamic viscosity at T_d, respectively. Since the variation of ρ with T_d is relatively negligible, $\mathrm{Re}(T_d)$ can be simplified as $\mathrm{Re}(T_d) = \rho UD_0/\mu(T_d)$. The well-known Vogel-Fulcher-Tammann (VFT) equation is commonly used to correlate variations of viscosity with temperature [60], which is expressed by

$$\mu(T_d) = A_\mu T_d^{1/2} \exp\left(\frac{B}{T_d - T_0}\right), \tag{4}$$

where A_μ is a prefactor, B is a quantity related to the activation barrier, and T_0 is the ideal transition temperature. The experimental results of dynamic viscosity as the ILs are heated agree well with the VFT equation (see Fig. S5 [45]). However, the precise relation between T_d and T_s is still unresolved in the literature due to the complex interplay between heat transfer, phase change, and impact dynamics. Future frontier studies are needed to measure T_d accurately and to validate the proposed power laws of $\beta_m(T_s) \sim \mathrm{Re}(T_d)^{1/4}$ and $\beta_m(T_s) \sim \mathrm{Re}(T_d)^{1/5}$ for low-viscous and high-viscous IL drop spreading, respectively.

IV. CONCLUSION

In summary, the impact dynamics of IL drops impacting on a heated flat surface are investigated experimentally. The results show that the IL drop impact events essentially comprise spreading (at low T_s), spreading with bubbling (at large T_s), and splashing with bubbling (at greater T_s and We for the IL with low values of μ and T_{onset}). Notably, the dynamic Leidenfrost effect leading to a complete rebound was not observed with the ionic liquids used. This absence can be explained by the low gas pressure generated by the evaporation and thermal decomposition, making ILs promising candidates for cooling and coating applications for the explored high T_s range. Moreover, the experimental fitting results show different β_m scaling laws: $\beta_m \sim \mathrm{Re}^{1/4}$ for low-viscosity ILs but $\beta_m \sim \mathrm{Re}^{1/5}$ for high-viscosity ILs on a flat surface at $T_s = 18\,^\circ\mathrm{C}$. These different power laws can be attributed to the viscous dissipation being dominant within the thin boundary layer next to the solid-liquid interface for the low-viscosity or within the bulk droplet for the high-viscosity IL drops.

ACKNOWLEDGMENTS

We acknowledge the funding support from the National Natural Science Foundation of China (12202032 and 51676010), as well as the Natural Sciences and Engineering Research Council of Canada Programs of Discovery (RGPIN-2020-05511) and Canada Research Chair (CRC TIER2 233147).

[1] J. Breitenbach, I. V. Roisman, and C. Tropea, Heat transfer in the film boiling regime: Single drop impact and spray cooling, Int. J. Heat Mass Transf. **110**, 34 (2017).

[2] G. Liang and I. Mudawar, Review of spray cooling—Part 1: Single-phase and nucleate boiling regimes, and critical heat flux, Int. J. Heat Mass Transf. **115**, 1174 (2017).

[3] G. Liang and I. Mudawar, Review of spray cooling—Part 2: High temperature boiling regimes and quenching applications, Int. J. Heat Mass Transf. **115**, 1206 (2017).
[4] J. Breitenbach, I. V. Roisman, and C. Tropea, From drop impact physics to spray cooling models: A critical review, Exp. Fluids **59**, 55 (2018).
[5] R. Andrade, O. Skurtys, and F. Osorio, Drop impact behavior on food using spray coating: Fundamentals and applications, Food Res. Intl. **54**, 397 (2013).
[6] A. Sankaran, J. Wu, R. Granda, V. Yurkiv, F. Mashayek, and A. Yarin, Drop impact onto polarized dielectric surface for controlled coating, Phys. Fluids **33**, 062101 (2021).
[7] A. Moreira, A. Moita, and M. Panao, Advances and challenges in explaining fuel spray impingement: How much of single droplet impact research is useful? Prog. Energy Combust. Sci. **36**, 554 (2010).
[8] X. Yang, L. Dai, and S.-C. Kong, Simulation of liquid drop impact on dry and wet surfaces using SPH method, Proc. Combust. Inst. **36**, 2393 (2017).
[9] X. Yang, M. Ray, S.-C. Kong, and C.-B. M. Kweon, SPH simulation of fuel drop impact on heated surfaces, Proc. Combust. Inst. **37**, 3279 (2019).
[10] D. Quéré, Leidenfrost dynamics, Annu. Rev. Fluid Mech. **45**, 197 (2013).
[11] C. Josserand and S. T. Thoroddsen, Drop impact on a solid surface, Annu. Rev. Fluid Mech. **48**, 365 (2016).
[12] G. Liang and I. Mudawar, Review of drop impact on heated walls, Int. J. Heat Mass Transf. **106**, 103 (2017).
[13] D. Lohse, Fundamental fluid dynamics challenges in inkjet printing, Annu. Rev. Fluid Mech. **54**, 349 (2022).
[14] V. Bertola, An impact regime map for water drops impacting on heated surfaces, Int. J. Heat Mass Transf. **85**, 430 (2015).
[15] T. Tran, H. J. J. Staat, A. Prosperetti, C. Sun, and D. Lohse, Drop Impact on Superheated Surfaces, Phys. Rev. Lett. **108**, 036101 (2012).
[16] L. Liu, Y. Zhang, G. Cai, and P. A. Tsai, High-speed dynamics and temperature variation during drop impact on a heated surface, Int. J. Heat Mass Transf. **189**, 122710 (2022).
[17] J. Breitenbach, I. V. Roisman, and C. Tropea, Drop collision with a hot, dry solid substrate: Heat transfer during nucleate boiling, Phys. Rev. Fluids **2**, 074301 (2017).
[18] G. Castanet, W. Chaze, O. Caballina, R. Collignon, and F. Lemoine, Transient evolution of the heat transfer and the vapor film thickness at the drop impact in the regime of film boiling, Phys. Fluids **30**, 122109 (2018).
[19] X. Zhang, Z. Zhu, C. Zhang, and C. Yang, Reduced contact time of a droplet impacting on a moving superhydrophobic surface, Appl. Phys. Lett. **117**, 151602 (2020).
[20] J. Guo, S. Lin, B. Zhao, X. Deng, and L. Chen, Spreading of impinging droplets on nanostructured superhydrophobic surfaces, Appl. Phys. Lett. **113**, 071602 (2018).
[21] H. Kim, U. Park, C. Lee, H. Kim, M. Hwan Kim, and J. Kim, Drop splashing on a rough surface: How surface morphology affects splashing threshold, Appl. Phys. Lett. **104**, 161608 (2014).
[22] T. Tran, H. J. Staat, A. Susarrey-Arce, T. C. Foertsch, A. van Houselt, H. J. Gardeniers, A. Prosperetti, D. Lohse, and C. Sun, Droplet impact on superheated micro-structured surfaces, Soft Matter **9**, 3272 (2013).
[23] L. Liu, G. Cai, and P. A. Tsai, Drop impact on heated nanostructures, Langmuir **36**, 10051 (2020).
[24] W. Zhang, T. Yu, J. Fan, W. Sun, and Z. Cao, Droplet impact behavior on heated micro-patterned surfaces, J. Appl. Phys. **119**, 114901 (2016).
[25] M. A. J. van Limbeek, P. B. J. Hoefnagels, M. Shirota, C. Sun, and D. Lohse, Boiling regimes of impacting drops on a heated substrate under reduced pressure, Phys. Rev. Fluids **3**, 053601 (2018).
[26] J. G. Leidenfrost, On the fixation of water in diverse fire, Int. J. Heat Mass Transf. **9**, 1153 (1966).
[27] M. Shirota, M. A. J. van Limbeek, C. Sun, A. Prosperetti, and D. Lohse, Dynamic Leidenfrost Effect: Relevant Time and Length Scales, Phys. Rev. Lett. **116**, 064501 (2016).
[28] G. C. Lee, H. Noh, H. J. Kwak, T. K. Kim, H. S. Park, K. Fezzaa, and M. H. Kim, Measurement of the vapor layer under a dynamic Leidenfrost drop, Int. J. Heat Mass Transf. **124**, 1163 (2018).
[29] S.-H. Lee, S. J. Lee, J. San Lee, K. Fezzaa, and J. H. Je, Transient dynamics in drop impact on a superheated surface, Phys. Rev. Fluids **3**, 124308 (2018).

[30] S.-H. Lee, M. Rump, K. Harth, M. Kim, D. Lohse, K. Fezzaa, and J. H. Je, Downward jetting of a dynamic Leidenfrost drop, Phys. Rev. Fluids **5**, 074802 (2020).
[31] J. M. Gordillo and G. Riboux, The initial impact of drops cushioned by an air or vapour layer with applications to the dynamic Leidenfrost regime, J. Fluid Mech. **941**, A10 (2022).
[32] I. U. Vakarelski, J. O. Marston, D. Y. C. Chan, and S. T. Thoroddsen, Drag Reduction by Leidenfrost Vapor Layers, Phys. Rev. Lett. **106**, 214501 (2011).
[33] M. Jiang, Y. Wang, F. Liu, H. Du, Y. Li, H. Zhang, S. To, S. Wang, C. Pan, J. Yu *et al.*, Inhibiting the Leidenfrost effect above 1, 000 °C for sustained thermal cooling, Nature (London) **601**, 568 (2022).
[34] C. M. Weickgenannt, Y. Zhang, S. Sinha-Ray, I. V. Roisman, T. Gambaryan-Roisman, C. Tropea, and A. L. Yarin, Inverse-Leidenfrost phenomenon on nanofiber mats on hot surfaces, Phys. Rev. E **84**, 036310 (2011).
[35] H. Kim, B. Truong, J. Buongiorno, and L.-W. Hu, On the effect of surface roughness height, wettability, and nanoporosity on Leidenfrost phenomena, Appl. Phys. Lett. **98**, 083121 (2011).
[36] G. V. V. Prasad, P. Dhar, and D. Samanta, Postponement of dynamic Leidenfrost phenomenon during droplet impact of surfactant solutions, Int. J. Heat Mass Transf. **189**, 122675 (2022).
[37] F. Celestini and G. Kirstetter, Effect of an electric field on a Leidenfrost droplet, Soft Matter **8**, 5992 (2012).
[38] Y. U. Paulechka, G. J. Kabo, A. V. Blokhin, O. A. Vydrov, J. W. Magee, and M. Frenkel, Thermodynamic properties of 1-butyl-3-methylimidazolium hexafluorophosphate in the ideal gas state, J. Chem. Eng. Data **48**, 457 (2003).
[39] C. Maton, N. De Vos, and C. V. Stevens, Ionic liquid thermal stabilities: Decomposition mechanisms and analysis tools, Chem. Soc. Rev. **42**, 5963 (2013).
[40] Y. Cao and T. Mu, Comprehensive investigation on the thermal stability of 66 ionic liquids by thermogravimetric analysis, Ind. Eng. Chem. Res. **53**, 8651 (2014).
[41] I. I. Sam, S. Gayathri, G. Santhosh, J. Cyriac, and S. Reshmi, Exploring the possibilities of energetic ionic liquids as non-toxic hypergolic bipropellants in liquid rocket engines, J. Mol. Liq. **350**, 118217 (2022).
[42] F. Heym, B. J. Etzold, C. Kern, and A. Jess, Analysis of evaporation and thermal decomposition of ionic liquids by thermogravimetrical analysis at ambient pressure and high vacuum, Green Chem. **13**, 1453 (2011).
[43] F. Zhang, X. Li, H. Li, J. Tang, G. Chen, L. Zhang, and G. Li, Dynamic study of [Emim] ac ionic liquid droplet impact on mildly heated solid surfaces, Int. Commun. Heat Mass Transfer **130**, 105783 (2022).
[44] P. Li, L. Yang, Q. Fu, and Z. Fang, Spray characteristics of the nanoparticle-containing gel propellants by using an improved single-phase nozzle, Fuel **315**, 122968 (2022).
[45] See Supplemental Material at http://link.aps.org/supplemental/10.1103/PhysRevFluids.8.073602 for the details of the experimental setup, the sequential snapshots of impact outcomes occurring for different ionic liquids, the phase diagrams of the impact outcomes for the [EMIM][BF4] and [BMIM][PF6] ionic liquid drops, the variation of dynamic viscosity, and the maximum spreading factor changing with temperature for the different ionic liquids..
[46] H. Almohammadi and A. Amirfazli, Droplet impact: Viscosity and wettability effects on splashing, J. Colloid Interface Sci. **553**, 22 (2019).
[47] A. Gauthier, J. C. Bird, C. Clanet, and D. Quéré, Aerodynamic Leidenfrost effect, Phys. Rev. Fluids **1**, 084002 (2016).
[48] W. Bouwhuis, R. C. A. van der Veen, T. Tran, D. L. Keij, K. G. Winkels, I. R. Peters, D. van der Meer, C. Sun, J. H. Snoeijer, and D. Lohse, Maximal Air Bubble Entrainment at Liquid-Drop Impact, Phys. Rev. Lett. **109**, 264501 (2012).
[49] P. Chantelot and D. Lohse, Leidenfrost Effect as a Directed Percolation Phase Transition, Phys. Rev. Lett. **127**, 124502 (2021).
[50] A.-L. Biance, C. Clanet, and D. Quéré, Leidenfrost drops, Phys. Fluids **15**, 1632 (2003).
[51] M. T. Clough, K. Geyer, P. A. Hunt, J. Mertes, and T. Welton, Thermal decomposition of carboxylate ionic liquids: Trends and mechanisms, Phys. Chem. Chem. Phys. **15**, 20480 (2013).

[52] C. Antonini, I. Bernagozzi, S. Jung, D. Poulikakos, and M. Marengo, Water Drops Dancing on Ice: How Sublimation Leads to Drop Rebound, Phys. Rev. Lett. **111**, 014501 (2013).
[53] Engineering Toolbox, Water-thermal conductivity vs. temperature, https://www.engineeringtoolbox.com/water-liquid-gas-thermal-conductivity-temperature-pressure-d_2012.html (2018).
[54] W. Chaze, O. Caballina, G. Castanet, and F. Lemoine, Spatially and temporally resolved measurements of the temperature inside droplets impinging on a hot solid surface, Exp. Fluids **58**, 96 (2017).
[55] N. Laan, K. G. de Bruin, D. Bartolo, C. Josserand, and D. Bonn, Maximum Diameter of Impacting Liquid Droplets, Phys. Rev. Appl. **2**, 044018 (2014).
[56] C. Clanet, C. Béguin, D. Richard, and D. Quéré, Maximal deformation of an impacting drop, J. Fluid Mech. **517**, 199 (2004).
[57] M. Pasandideh-Fard, Y. Qiao, S. Chandra, and J. Mostaghimi, Capillary effects during droplet impact on a solid surface, Phys. Fluids **8**, 650 (1996).
[58] X. Zhang, B. Ji, X. Liu, S. Ding, X. Wu, and J. Min, Maximum spreading and energy analysis of ellipsoidal impact droplets, Phys. Fluids **33**, 052108 (2021).
[59] S. Wildeman, C. W. Visser, C. Sun, and D. Lohse, On the spreading of impacting drops, J. Fluid Mech. **805**, 636 (2016).
[60] U. Domańska and M. Królikowska, Density and viscosity of binary mixtures of thiocyanate ionic liquids + water as a function of temperature, J. Solution Chem. **41**, 1422 (2012).